ROYAL SOCIETY OF CHEMISTRY

PCCP

PAPER

View Article Online
View Journal | View Issue

Cite this: *Phys. Chem. Chem. Phys.*, 2022, **24**, 14044

Single-photoelectron collection efficiency in 4D ultrafast electron microscopy

Wyatt A. Curtis,[ab] Simon A. Willis[ab] and David J. Flannigan *[ab]

Received 15th March 2022,
Accepted 25th May 2022

DOI: 10.1039/d2cp01250b

rsc.li/pccp

In femtosecond (fs) 4D ultrafast electron microscopy (UEM), a tradeoff is made between photoelectrons per packet and time resolution. One consequence of this can be longer-than-desirable acquisition times for low-density packets, and particularly for low repetition rates when complete photothermal dissipation is required. Thus, gaining an understanding of photoelectron trajectories in the gun region is important for identifying factors that limit collection efficiency (CE; fraction of photoelectrons that enter the illumination system). Here, we continue our work on the systematic study of photoelectron trajectories in the gun region of a Thermo Fisher/FEI Tecnai Femto UEM, focusing specifically on CE in the single-electron regime. Using General Particle Tracer, calculated field maps, and the exact architecture of the Tecnai Femto UEM, we simulated the effects of fs laser parameters and key gun elements on CE. The results indicate CE strongly depends upon the laser spot size on the source, the (unbiased) Wehnelt aperture diameter, and the incident photon energy. The CE dispersion with laser spot size is found to be strongly dependent on aperture diameter, being nearly dispersionless for the largest apertures. A gun crossover is also observed, with the beam-waist position being dependent on the aperture diameter, further illustrating that the Wehnelt aperture acts as a simple, fixed electrostatic lens in UEM mode. This work provides further insights into the operational aspects of fs 4D UEM.

Introduction

Femtosecond (fs) laser-based pulsed-beam transmission electron microscopy (called 4D ultrafast electron microscopy, UEM) can reach sub-picosecond timescales and has been used to conduct ultrafast pump–probe imaging, diffraction, and element-specific spectroscopy.[1–11] For this approach, the pulsed electron beam is typically generated with fs UV pulses and has been successfully extended to all standard gun types used in commercial electron-microscope platforms.[1,2,6,12–18] Indeed, it has been shown that both single-shot nanosecond imaging and stroboscopic picosecond imaging can be done with the identical thermionic electron gun, the same cathode, and without the need to adjust the electric fields around the emitter (base instrument was an FEI Tecnai T12).[19,20] Properties of the photoelectron packets – and thus the achievable resolutions – can be controlled to some extent with the pulsed laser (*e.g.*, through photon energy, pulse fluence, pulse duration, and laser spot size) and characterized with spectroscopy and cross-correlation methods.[3,6,8,11,12,14,17,21–26]

A key parameter dictating the manner in which materials and phenomena can be studied with UEM is the laser repetition rate (f_{rep}).[9,12,19,21] Unlike for molecular beams or liquid flow cells, the specimen region in UEM is typically not refreshed prior to arrival of the next photoexcitation pulse. Thus, care must be taken not to induce specimen changes that are temporally long lived compared to $f_{\mathrm{rep}}{}^{-1}$. That is, one ideally wants the time between packets ($f_{\mathrm{rep}}{}^{-1}$) to be longer than the full specimen recovery time (τ_{rep}; *e.g.*, electron and lattice thermalization and complete thermal dissipation). This is to avoid creating new long-lived phases or producing irreversible degradation, such as plastic deformation, fracture, or melting. Identifying and using such an f_{rep} – which is material, specimen, and photoexcitation dependent – also enables consistent excitation of the same initial state, such as the ground state.

The thin, electron-transparent specimens required for UEM experiments (as with TEM experiments) pose challenges for achieving complete photothermal heat dissipation between excitation pulses for high f_{rep}. However, while operating at the minimum-possible f_{rep} may be preferred for the reasons noted above, beam current is commensurately reduced with lowering f_{rep} (and with all else remaining the same) such that longer acquisition times are needed to reach usable signal levels and contrast strengths. Like with TEM, longer acquisition times can limit resolution due to specimen drift and lab instabilities, system fluctuations, and detector and background

---

[a] *Department of Chemical Engineering and Materials Science, University of Minnesota, 421 Washington Avenue SE, Minneapolis, MN 55455, USA. E-mail: flan0076@umn.edu; Tel: +1 612-625-3867*

[b] *Minnesota Institute for Ultrafast Science, University of Minnesota, Minneapolis, MN 55455, USA*

signal noise. Beyond creating an extremely stable lab environment, one method for mitigating this is to increase the incident laser pulse fluence and thus the number of photoelectrons per packet for a given f_{rep}. This, however, can lead to deleterious space-charge effects, a reduction in coherence, and thus a reduction in spatiotemporal resolution.[6,11,21,22]

Intuitively, one anticipates optimum beam quality at the lowest-possible acquisition time for a given photon energy ($h\nu$) to be achieved when operating in the so-called single-electron regime, wherein each packet is populated with, on average, one photoelectron.[1,22,27] In principle, this entirely avoids particle–particle interactions while providing the highest current at a given f_{rep} for a space-charge-free regime. However, this implies that low f_{rep} experiments can be reliably conducted only at low magnifications due to the commensurately long acquisition times and increased blurring due to drift and mechanical/field instabilities. Indeed, high-magnification fs pulsed-beam photoelectron images (*i.e.*, resolved features smaller than 1 nm) have been generated with $f_{\text{rep}} \geq 200$ kHz ($f_{\text{rep}}^{-1} \leq 5$ μs) and with acquisition times spanning seconds to minutes.[2,12,15,18,28] Importantly, however, ultimate quantitative limits of the high-resolution parameter space, particularly for low f_{rep} experiments, have yet to be established for true pump–probe fs UEM imaging (*i.e.*, with specimen photoexcitation); speculative predictions suggest that no better than 1 nm will be possible, regardless of f_{rep}.[6] Though for the predicted photon-induced near-field (*i.e.*, PINEM) aberration, deconvolution of the annular chromatic point spread function should recover the otherwise obscured details.[3,24,25] As an interesting aside, very few ultrafast pump–probe UEM experiments have been conducted in the weak-excitation regime, where low-fluence pump pulses ($F \sim$ μJ cm^{-2}) induce "dilute" dynamics that are then probed at high f_{rep} common to laser oscillators and beam-blanker pulsers.[1,19,27,29–37]

The main challenges associated with conducting high-resolution UEM (HR-UEM) studies of fs–ps atomic, molecular, and nanoscale materials dynamics seem clear. Accordingly, a path forward involving systematic and increasingly complex modeling and simulations targeted at optimization can be designed.[22,38] However, the complexity of the instruments and the variety of cathode materials, shapes, and gun types necessitates a thorough, rigorous approach to the development of a quantitative and comprehensive understanding of pulsed-beam behavior in modified commercial instruments.[12,16,21,39] Indeed, one must contend with particle–particle and particle–field interactions, the precise fields and geometries of all elements comprising the TEM, the properties and behaviors of the laser system, and the unconventional manner in which the TEM is operated when in UEM mode, in addition to lab-specific and laser instabilities.

Accordingly, there are significant opportunities to identify and understand the influence of key elements and effects, as well as simple (low-cost) areas of improvement and optimization.[12,21] In fact, despite fs UEM – defined here as coupling of a fs laser with an otherwise conventional TEM – having been under earnest development and application for nearly 20 years,[1] there is still much to understand about the fundamental behaviors and performance metrics. This is not surprising considering the history of analogous (and still ongoing) efforts dedicated to the more mature methods of ultrafast electron diffraction (UED) and dynamic (nanosecond single-shot) TEM and especially considering the relative simplicity of dedicated UED instruments.[21,40,41] In fact, one can look to the arc of development of high-resolution TEM, normalized by the associated monetary investment and activity level, to estimate an analogous trajectory for the development of HR-UEM.[42–47]

Owing to the opportunities noted above, we have initiated an effort to fully and completely characterize and quantify the behavior of single-electron packets in a Thermo Fisher/FEI Tecnai Femto UEM paired with a Light Conversion PHAROS fs pulsed laser, which is the system installed at the University of Minnesota within the Minnesota Institute for Ultrafast Science. One aspect of this effort includes simulating single-electron trajectories for the exact architecture and elements of the Tecnai Femto gun region† (*i.e.*, from the electron source to the X-ray aperture) using particle tracing software and calculated field maps. Once complete, we envision modifying and extending these methods to multi-electron packets and to the entire microscope column – from source to detector. We are first focusing on mapping the single-electron regime, which hypothetically should provide the highest resolutions, all else being the same.[1,6,21,22] Further, it is our hope that the approach and methods we develop, and the insights we glean, can be extended to other systems, thus serving as a useful foundation upon which to build specific descriptions and resolution-focused, operational "phase diagrams" for modality optimization.[6,12]

We have divided our initial effort specific to the electron gun region into three interrelated but conceptually distinct Focus Areas: (1) temporal resolution, (2) collection efficiency (*i.e.*, beam current), and (3) beam coherence. Such a segmented approach allows us to simplify the design of the work, focus our efforts, and compartmentalize the large body of results. We have previously described our findings for single-electron temporal resolution in the gun region (Focus Area 1).[38] Among other insights, results of the simulations indicate that the statistical electron packet duration can be controlled not only with laser pulse duration and Wehnelt bias,[6,12] but also with laser spot size, (unbiased) Wehnelt aperture diameter, and incident photon energy (for a fixed work function). This is in addition to the cathode-to-Wehnelt aperture distance.[12,48]

Here, we now focus on simulating and calculating the collection efficiency in the single-electron regime (Focus Area 2). We define collection efficiency (CE) as the fraction of photoemitted electrons that pass through the X-ray aperture and enter the illumination (condenser) system. Accordingly, the CE will range between 0 and 1, with 1 indicating that each photoelectron generated at the source passes through the X-ray aperture. The importance of CE to optimizing UEM beam current and minimizing acquisition time is clear and has been previously noted.[6,48] As we illustrate here, and as we found in

---

† Provided by Dr Erik Kieft at Thermo Fisher Scientific.

the temporal resolution study, parameters such as laser spot size on the source (and the resulting distribution of transverse momenta), and the Wehnelt aperture diameter, have a significant impact on the overall behaviors for even the single-electron regime.[12,38] Indeed, enhanced coupling of single electrons into the illumination system may occur even for an unbiased Wehnelt electrode and an otherwise unmodified TEM, though much additional work is needed, especially for multi-electron packets.[6,49]

Experimental

The elements and dimensions of the Tecnai Femto gun region, as well as the software tools and simulation methods, are the same as those used in the single-electron temporal resolution study.[38] Nevertheless, they are again described here for convenience. Particle tracing simulations were conducted using General Particle Tracer (GPT, Pulsar Physics) and cylindrically symmetric field maps calculated with Poisson Superfish.[50,51] GPT is used to solve the relativistic equations of motion with a fifth-order embedded Runge–Kutta solver and to calculate the Lorentz force acting on the particle. Poisson Superfish consists of a finite element method used to solve Poisson's equation for electrostatics. The exact architecture and dimensions for the gun region of the Thermo Fisher/FEI Tecnai Femto UEM (base instrument is a Tecnai T20 G2) comprised the physical elements (Fig. 1a). The key parameters of interest in the gun were the Wehnelt aperture diameter (D_W, varied), the LaB$_6$ tip diameter (D_{tip}, mainly fixed at 180 μm but varied for one set of simulations), and the aperture-to-tip distance (Z_{tip}, fixed at 350 μm).[48] In UEM mode, the Wehnelt triode is unbiased in the Tecnai Femto and thus acts as a simple, fixed electrostatic lens. Indeed, this is one motivator for conducting detailed simulations of the Tecnai Femto UEM – we seek to quantitatively determine the effect of an unbiased Wehnelt triode on photoelectron packet properties and behaviors.[6,38,49]

Photoemission spot size is defined as a Gaussian laser spot size (fwhm) on the cathode surface.[1,38] Here, only photoemission from the flat surface is simulated (Fig. 1b), a configuration that can be achieved experimentally by focusing the laser, by using a LaB$_6$ (or other material) cathode where D_{tip} is larger than the laser spot size, or by using a cathode with a non-emissive guard ring.[1,11,12,16] For some simulations, the photoemission spot size was fixed at 50 μm, the laser spot sized typically used in the University of Minnesota UEM lab.[52] To reduce computation time, and to be consistent with the temporal resolution study, simulations were conducted with $n = 5 \times 10^4$ non-interacting particles generated from the cathode along a Gaussian temporal profile set to be $\tau_{laser} = 300$ fs (fwhm). Thus, each data point is the integrated result of the spatial Gaussian distribution (*i.e.*, the photoemission probability distribution, Fig. 1b) of 5×10^4 non-interacting particles. The emitted trajectory probability distribution from the cathode [$P(\theta)$] was set to follow a $\cos(\theta)$ behavior azimuthally integrated over an angle φ (Fig. 1c).[48,53] Again, we did this in order to remain consistent with

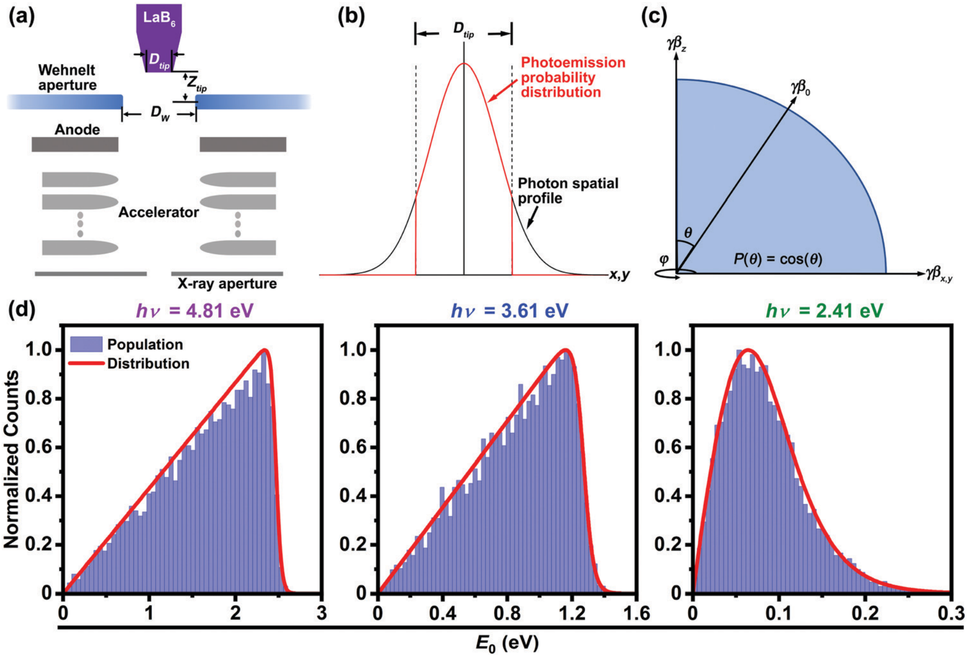

Fig. 1 Overview of the simulation elements. (a) Simplified schematic of the Tecnai Femto electron gun with key elements and dimensions labeled (not to scale). (b) Representative photoemission probability distribution for the case where the Gaussian laser spot size (*i.e.*, photon spatial profile) is larger than the LaB$_6$ tip diameter (D_{tip}). (c) Photoemission probability (P) as a function of emission angle (θ) relative to the optical axis of the electron gun. An emission angle of zero corresponds to a trajectory parallel to the optical axis and a maximum emission probability. γ and β are the Lorentz factor and the normalized relativistic velocity, respectively. Their product is the rest-mass-normalized particle momentum used in GPT. (d) Calculated normalized initial photoelectron kinetic energy (E_0) distributions for $h\nu$ = 4.81, 3.61, and 2.41 eV (left, middle, and right, respectively). Reproduced from ref. 38 with permission from the PCCP Owner Societies.

the temporal resolution study.[38] The nature of the initial distribution will affect the CE, mainly due to interactions of the off-axis photoelectrons with the Wehnelt aperture. Thus, it is important to use a consistent approach despite the cos(θ) distribution not being employed universally.[54–56]

Photoelectrons generated at the LaB_6 source are accelerated from initial kinetic energies (E_0) dictated by the incident photon energy ($h\nu$) to 200 keV along the accelerator region before reaching the X-ray aperture (Fig. 1a). Here, the LaB_6 work function was fixed at Φ = 2.4 eV.[57] (Note that Φ for LaB_6 is sensitive to a number of factors – use of a different value here will only lead to a commensurate rescaling of the findings. The specific number used in the simulations is less important than the observed trends.) Thus, different distributions of E_0 will result for the different values of $h\nu > \Phi$ simulated here (Fig. 1d). The distributions were modeled as transmission coefficients for a free electron encountering a step potential, and photoemission was approximated by shifting the Fermi–Dirac distribution by the $h\nu$ energy of the incident photon, following the approach taken by Mogren and Reifenberger for LaB_6.[58] Note again that because we are presently focused on the gun region, the X-ray aperture is the final limiting element in the simulations. Electron packet populations were collected at a virtual screen positioned 35 cm from the photoemission plane. At this position, all electrons have been fully accelerated, have kinetic energies of 200 keV, and have propagated past the X-ray aperture plane.[38]

Results and discussion

Unbiased Wehnelt aperture interaction strength

A key parameter for determining the Wehnelt-aperture lensing behavior is the beam radius in the aperture plane. As described in the Experimental section, the Wehnelt aperture is at zero bias relative to the photoemitter (−200 kV) and thus acts as a weak electrostatic lens in the tip region of the electron gun. Nevertheless, emitted electrons experience repulsive transverse forces that depend on D_W and the beam radius in the aperture plane. Fig. 2 shows the calculated spatial distributions of the magnitudes of the transverse electric fields ($|E_r|$) in the tip region of the electron gun for D_W = 0.7 and 1.0 mm. As can be seen, the D_W = 0.7 mm aperture generates a field distribution that permeates further into the footprint of D_{tip}. In addition, the electric-field gradient is steeper within this footprint for the smaller aperture. Accordingly, off-axis photoelectrons experience a stronger field gradient for smaller apertures and a given cathode size. Indeed, the difference in transverse displacements of the electrons is on the order of millimeters for the different aperture diameters (see below). Further, larger apertures provide a larger field-free region centered on the optical axis, in addition to generating a more expansive electric field overall – for example, compare the $|E_r|$ values spanning the 180 μm centered at R = 0 μm for the Z = 1 mm positions in Fig. 2a and b. No temporal broadening occurs within this field-free region.[38]

Two main factors affect beam radius in the Wehnelt aperture plane: (1) the initial emission point relative to the optical axis (*i.e.*, the position relative to R = 0), and (2) the initial electron kinetic energy, E_0. The first factor is a direct modulation of the initial spot size of the electron beam (determined by the laser spot size on the cathode). The second factor can be understood by noting that electrons with higher E_0 have larger transverse momenta, thus leading to a relative increase in the initial integrated packet divergence. The effect these factors have on CE can be illustrated by considering single electrons emitted from R = 45 μm and R = 90 μm with E_0 = 2.40 eV and with initial trajectories normal to the Wehnelt aperture. For the D_W = 1.0 mm aperture, the difference in $|E_r|$ in the aperture plane at these two positions is 0.21 MV m^{-1}. Assuming

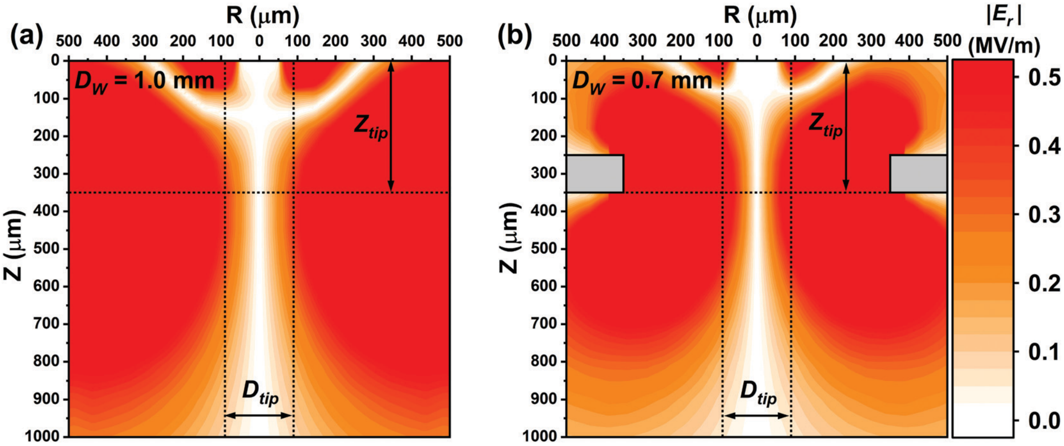

Fig. 2 Electric field contour maps in the vicinity of the unbiased Wehnelt aperture for (a) D_W = 1.0 mm and (b) D_W = 0.7 mm. The horizontal dotted line at Z = 350 μm marks the position of the outer face of the Wehnelt aperture (relative to the emitter surface at Z = 0 μm). This defines the Z_{tip} dimension. The vertical dotted lines mark the edges of the cathode surface and thus define the D_{tip} dimension (180 μm diameter). The color bar displays the scale of the electric-field magnitude, $|E_r|$. The grey rectangles centered at Z = 300 μm in (b) represent the Wehnelt aperture edges, which extend out to R = 350 μm; the aperture edges are flush with the vertical borders in (a).

constant Wehnelt interactions and no transverse acceleration by the accelerating field, the calculated difference in transverse displacement is 8 mm after 2 ns of propagation (roughly the gun escape time). This is a significant displacement and indicates the more strongly-deflected electron will not pass through the X-ray aperture (diameter < 8 mm), thus illustrating the impact on CE. Also note that electrons with higher E_0 have larger longitudinal momenta, on average, which shortens the residence time in the aperture transverse fields leading to a weaker convergence. Having established the general effects of an unbiased Wehnelt electrode, the effects of specific electron-gun elements and laser parameters on CE are now considered.

Dependence of CE on photoemission spot size for key values of D_W

As was done in the temporal resolution study,[38] we first established baseline behaviors for single-electron CE by simulating three key and discrete initial photoelectron kinetic energies (E_0 = 0.10, 1.76, and 2.40 eV) for D_W = 0.7 and 1.0 mm. Beginning by using three discrete energies instead of the distributions shown in Fig. 1d serves as a first approximation to the more complex but also more realistic cases. As can be seen in Fig. 3, a strong dependence of CE on photoemission spot size and D_W is generally observed; CE decreases with increasing spot size for both values of D_W. However, precise behaviors for each of the E_0 values vary and strongly depend upon D_W. First, while the behaviors for each of the E_0 values are identical for D_W = 0.7 mm (Fig. 3, top panel), the E_0 = 0.10 eV energy deviates significantly from the 1.76 and 2.40 eV energies for D_W = 1.0 mm (Fig. 3, bottom panel). Second, while CE = 1.0 for all E_0 at spot sizes below 5 μm for D_W = 0.7 mm, only the 0.10 eV energy shows a CE = 1.0 (for spot sizes below 20 μm) for the 1.0 mm aperture. The higher E_0 energies attain maximum CE values between 0.33 (2.40 eV) and 0.38 (1.76 eV). Third and finally, while CE rapidly decreases to below 0.01 with increasing spot size for all E_0 for D_W = 0.7 mm, the lowest value for D_W = 1.0 mm is 0.14 for E_0 = 2.40 eV.

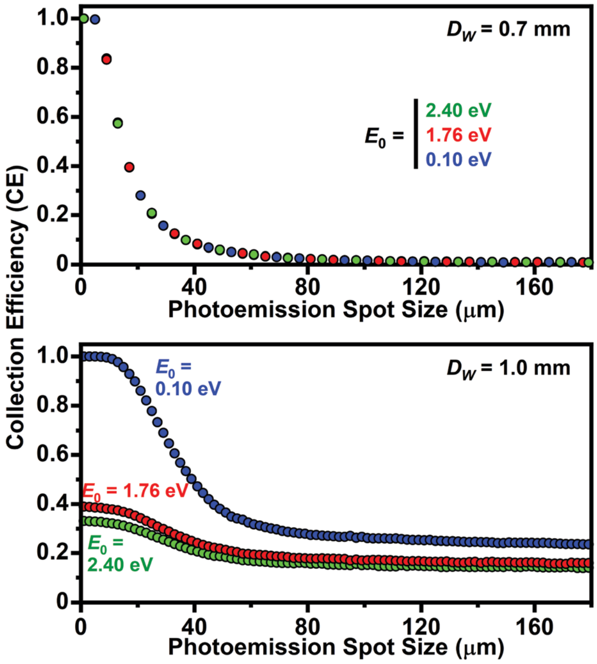

Fig. 3 Single-electron-packet collection efficiency (CE) as a function of photoemission spot size for three discrete values of E_0 for D_W = 0.7 mm (top panel) and 1.0 mm (bottom panel).

The general behaviors shown in Fig. 3 again arise from the Wehnelt aperture acting as a weak, fixed electrostatic lens when in UEM mode (*i.e.*, absent feedback biasing). As such, the distance of an electron from the center x, y = 0, 0 position in the plane of the Wehnelt aperture – which is determined by the initial photoemission position and momentum – determines the transverse electric-field strength experienced by the propagating electron. Note that here we are assuming a perfectly flat LaB_6 emitting surface; initial trajectories from actual cathodes will be more complex owing to surface roughness, structural and compositional evolution with time, and adsorption of contaminating species.[57,59–61] Here, we observe that the divergence of an electron after the Wehnelt aperture scales with photoemission spot size, which then impacts the integrated transverse packet radius (parameterized here as the fwhm diameter, D_{packet}) as it is accelerated toward the X-ray aperture. Accordingly, one would expect a larger fraction of the total population exiting the Wehnelt to ultimately be blocked by the X-ray aperture for larger photoemission spot sizes; these electrons will not enter the illumination system, and the CE will be reduced.

Overall, the simulation results indicate that both the single-electron CE and the temporal resolution can be improved by reducing the photoemission spot size for a given D_W (*i.e.*, by creating a tighter laser focus on the LaB_6 surface while in the single-electron regime).[12,38] Possible practical avenues for further reducing the photoemission spot size on the source could involve expansion of the laser spot diameter on the final focusing lens (limited by clipping requirements along the beam path) or redesign of the internal laser path to minimize the distance between the final lens and the photocathode. As an aside, we hypothesize that this also may have implications for the ideal electron source shape for laser-driven UEM.[21] Note also that CE values of 1.0 for certain gun configurations have been previously predicted,[48] which has significant implications for the role of aperturing and reductions in beam current in the condenser system – this is a key area of interest for future work. As shown below, regimes with CE values of 1.0 are also predicted to exist when considering the full E_0 distribution (Fig. 1d), even for $h\nu$ = 4.81 eV and Φ = 2.4 eV. However, full system simulations are required to gain insights into the fraction of photoelectrons making it to the specimen and to the detector.

Energy filtering and the presence of a gun crossover

The difference in CE at a select spot size for discrete E_0 values for D_W = 1.0 mm shown in Fig. 3 (bottom panel) suggests that a serendipitous energy filtering effect is at work in the gun region. This filtering leads to a narrowing of the electron-energy distribution arising from preferential aperturing of electrons with higher initial kinetic energies, analogous to aperturing the beam further down the column. The potential origins of this effect can be illustrated by analyzing a simulation of the transverse beam properties for a fixed E_0 and a fixed photoemission spot size as electrons exit through Wehnelt apertures of various D_W (Fig. 4). Here, we chose E_0 = 1.76 eV and a photoemission spot size of 50 μm. We simulated how the packet diameter, D_packet, evolves from the LaB$_6$ surface ($Z = 0$) to a longitudinal position $Z = 10$ mm for D_W ranging from 0.7 mm to 1.2 mm. Note that all gun elements within this longitudinal distance were included in the simulation despite not being explicitly shown in the figure.

Several notable behaviors emerge from the beam dynamics simulations summarized in Fig. 4. First, while D_packet initially increases upon moving away from the LaB$_6$ surface ($Z = 0$), the smaller diameter apertures show a noticeable decrease in D_packet before reaching the aperture plane (Z = 0.35 mm; see, for example, D_W = 0.7 mm). Second, while D_packet appears to be always increasing for $D_\mathrm{W} > \sim 0.9$ mm and $Z \leq 0.35$ mm, smaller aperture values show a decrease before reaching the aperture plane. Third, all values of D_packet except for the 1.2 mm aperture continue to decrease once past the aperture plane before again increasing. This reduction in D_packet once past the aperture results in a beam waist, w_0, generally positioned within 3 mm of the source surface and increasing in size with increasing D_W. This is indicative of a crossover and occurs for aperture sizes less than 1.2 mm, despite the Wehnelt being unbiased. Further, the Z position of w_0 (*i.e.*, the crossover point, Z_{w_0}) shows an increase and then decrease in going from 0.7 to 1.1 mm. Fourth, the smaller apertures show stronger divergence to larger D_packet for $Z > Z_{w_0}$. Generally, these behaviors are dictated by the resulting proximity and thus the transverse electric field magnitude experienced by the statistical photoelectron packet. Accordingly, reducing the photoemission spot size for a given D_W has the same basic effect as increasing D_W for a given spot size; Z_{w_0} will first increase and then decrease, and the divergence to larger D_packet for $Z > Z_{w_0}$ will go down.

Having established the behavior of D_packet for $Z \leq 10$ mm from the LaB$_6$ surface for a single initial kinetic energy, we next simulated and compared the beam waist position (*i.e.*, crossover position) and size for all three discrete values of E_0 shown in Fig. 3, again for a photoemission spot size of 50 μm. Fig. 5 shows a summary of the results for D_W = 0.7 to 1.2 mm. Note that no crossover occurs for the specific cases of E_0 = 1.76 and 2.40 eV and D_W = 1.2 mm. In these cases, D_packet continuously expands as it propagates from the cathode surface to Z = 10 mm, indicating that interactions with the aperture field are too weak to induce a dramatic change in transverse momentum. While the general behaviors of Z_{w_0} and w_0 are similar for each E_0, two obvious trends can be seen. First, the increasing and decreasing behavior of Z_{w_0} with increasing D_W, as seen in Fig. 4, occurs for each energy, but the maximum value of Z_{w_0} for all simulated apertures increases with decreasing E_0 (Fig. 5, top panel). This shows that, for a given D_W and photoemission spot size, the crossover point of initially higher energy photoelectrons will be positioned closer to the Wehnelt aperture – a range of crossover points will be present for a range of E_0. Second, again as seen for E_0 = 1.76 eV in Fig. 4, w_0 steadily increases with increasing D_W,

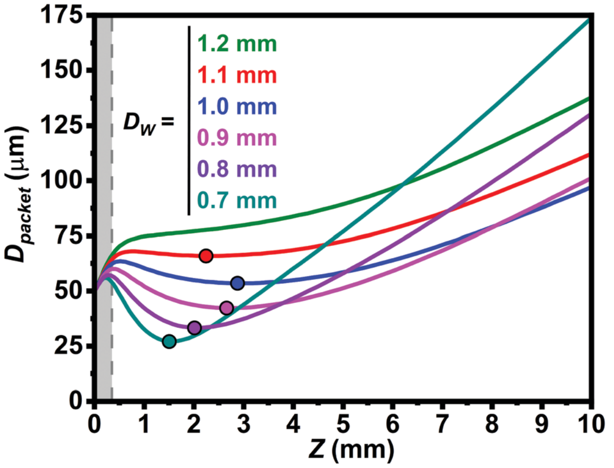

Fig. 4 Evolution of photoelectron packet diameter (D_packet) for a 50 μm laser spot size, for E_0 = 1.76 eV, and for Wehnelt aperture diameters (D_W) ranging from 0.7 mm to 1.2 mm. The LaB$_6$ cathode surface is at Z = 0, and the grey shaded region denotes the Z_tip region (see Fig. 1a). The dashed grey line is the plane of the Wehnelt aperture. The colored dots mark the beam waists (w_0) for each aperture size and were found with a first-derivative analysis of the beam diameter in MATLAB.

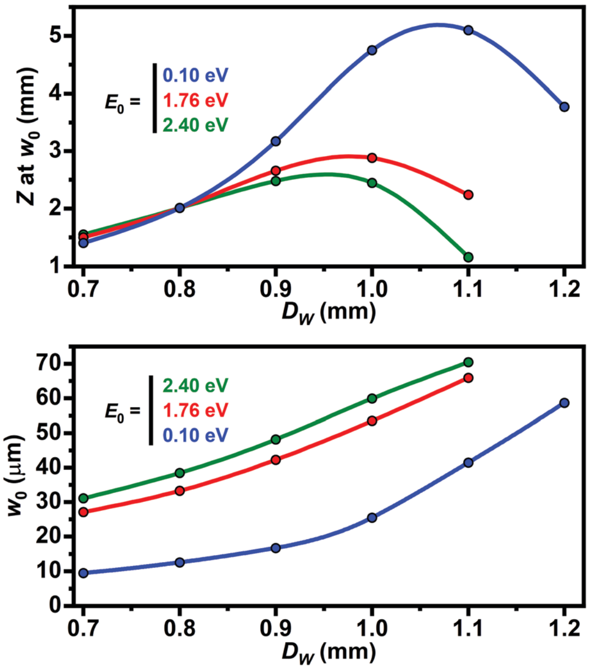

Fig. 5 Photoelectron beam waist behavior as a function of Wehnelt aperture size for three discrete initial kinetic energies. The top panel shows the crossover position (Z_{w0}) between the cathode surface and Z = 10 mm from the surface, while the bottom panel shows how w_0 varies, both as a function of D_W for the initial kinetic energies noted. The solid curves are spline interpolations of the individual points and are included to guide the eye and to show the general trends. Here, w_0 and the crossover position were found with a first-derivative analysis of beam diameter in MATLAB.

with higher kinetic energy photoelectrons generally having larger beam waists for a given aperture diameter (Fig. 5, bottom panel).

The behaviors shown in Fig. 5 arise from effects of a lower initial deviation of transverse momentum for the lower kinetic energy photoelectrons – the interaction strength with the aperture field can be qualitatively appreciated by noting how the position and size of w_0 for each E_0 shift relative to one another. That is, the resulting crossover properties are entirely contingent upon how the photoelectrons are lensed by the unbiased Wehnelt aperture. While the photoemission spot size is fixed, D_{packet} clearly varies as the photoelectrons are accelerated toward the X-ray aperture (see Fig. 4). For a given E_0, reduced values of D_W create smaller packet diameters at the aperture plane – this again can be seen by inspecting the $Z = 0.35$ mm position in Fig. 4 for $E_0 = 1.76$ eV. As noted above, increasing DW has the same basic effect as reducing the size of the photoelectron beam for a fixed aperture size. This is because the interaction strengths are reduced due to simple proximity arguments. As illustrated in Fig. 5, this is also the case for varying initial kinetic energies – fewer photoelectrons are strongly impacted by electrostatic lensing at lower initial kinetic energies because the initial deviation in transverse momentum is commensurately lower. Note that the increase in slope for each E_0 above $D_W \sim 0.9$ mm is also an indication of how the populations are shifting toward weaker overall interactions, with lower E_0 being impacted to a greater degree, as expected (Fig. 5, lower panel).

CE as a function of D_W for a fixed laser spot size

Having identified the presence of a gun crossover and an energy filtering effect, we next analyzed the simulated trajectories for the entire gun region (*i.e.*, from source to X-ray aperture) in order to determine the behavioral dependence of CE on D_W. The electron-packet parameters were the same as those shown in Fig. 3. The photoemission spot size was fixed at 50 μm, while D_W was varied from 0.7 to 1.2 mm. As can be seen in Fig. 6, while all three discrete values of E_0 show an increase in CE with increasing D_W, the higher energies reach maximum values of only 0.23 and 0.27 at $D_W = 1.2$ mm ($E_0 = 2.40$ and 1.76 eV, respectively). Comparatively, the $E_0 = 0.10$ eV energy reaches a value of 0.95. Note, however, that CE *vs.* D_W generally shows a sigmoidal response indicating that values of $D_W > 1.2$ mm will result in little or no additional increase in CE, regardless of E_0. Indeed, the higher energies show increases in CE of only ∼0.4% in going from $D_W = 1.1$ to 1.2 mm. Conversely, for the smallest diameters simulated (0.7 and 0.8 mm), CE is nearly identical for all values of E_0; clear deviations begin to appear for $D_W > 0.8$ mm.

As with the other simulated behaviors, the trends shown in Fig. 6 can be explained by considering the interaction strength between the Wehnelt-aperture field and the photoelectrons. For example, a decreased interaction strength, as occurs for larger aperture sizes (or smaller laser spot sizes) and lower E_0, results in a larger number of initially off-axis photoelectrons (*i.e.*, those not emitted from the $x, y = 0, 0$ LaB_6 center position) passing through the X-ray aperture. This can be understood by recognizing that photoelectrons with lower E_0 values have on average lower transverse velocities, which leads generally to a decrease in interaction strength with the aperture. For the parameter space explored here (*e.g.*, 50 μm spot size), this appears to be true for $D_W > 0.8$ mm, where CE becomes dependent on E_0. One might conclude from this that there is a combined D_W and spot-size threshold value for CE divergence based on E_0 that shifts to smaller aperture sizes for smaller laser spot sizes. Note, however, that the electrostatic field strength in the plane of the Wehnelt aperture becomes increasingly uniform with decreasing D_W (see Fig. 2). Thus, using smaller laser spot sizes with small Wehnelt apertures only produces an overall increase in CE, independent of E_0 (see Fig. 3). That is, the x, y position of photoemission from the source determines if the photoelectron will be deflected by the Wehnelt-aperture electrostatic field, independent of transverse momentum. Overall, this shows that higher values of CE are found for lower E_0 and for larger D_W, as expected from the results already discussed. As importantly, however, smaller apertures can be used in conjunction with smaller laser spot sizes to generate dramatically improved beam currents and perhaps also improved coherence, potentially at the cost of temporal resolution.[38]

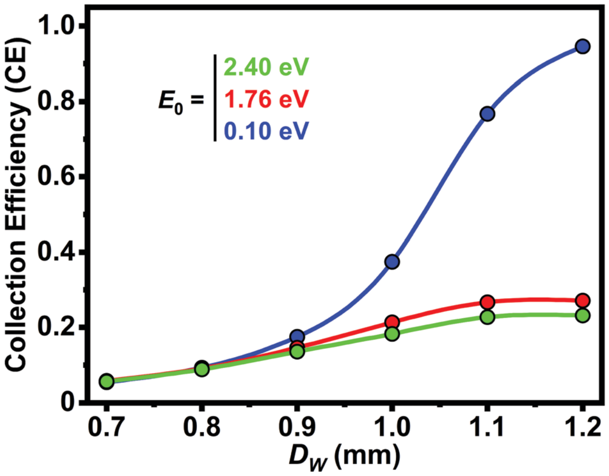

Fig. 6 Collection efficiency (CE) as a function of Wehnelt aperture diameter (D_W) for three discrete values of E_0 and a photoemission spot size of 50 μm.

CE for an *hν*-determined E_0 distribution for $\Phi = 2.4$ eV

To this point, we have simulated discrete values of E_0 in order to determine baseline behaviors. While useful, behaviors based on the distributions shown in Fig. 1d are expected to more accurately reflect experiments. Thus, we repeated the simulations shown in Fig. 3 for a range of D_W but this time using the E_0 distribution generated with $h\nu = 4.81$ eV, the results of which are summarized in Fig. 7. All other parameters were kept the same. As was the case for the discrete values of E_0, a general decrease in CE was observed with increasing photoemission spot size for all D_W. Further, the effect was weakened for larger D_W, again as generally seen for discrete values of E_0 – the smallest apertures showed the largest CE dispersion behaviors, with the effects being dramatically decreased with increasing

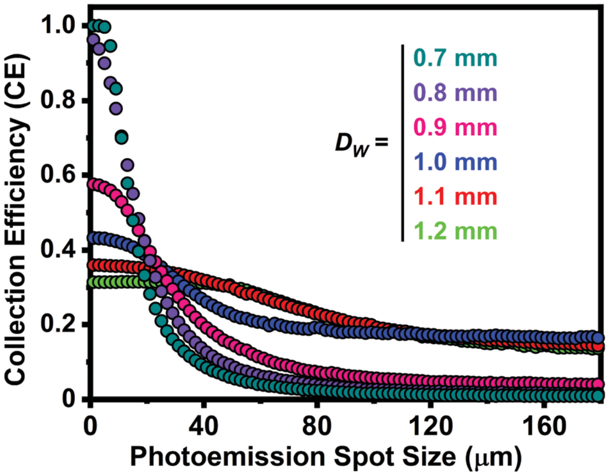

Fig. 7 Collection efficiency (CE) as a function of photoemission spot size for a range of Wehnelt aperture diameters (D_W) for the $h\nu$ = 4.81 eV E_0 distribution (see Fig. 1d).

D_W. In addition, CE is very roughly the same (~0.33) for all aperture diameters at a photoemission spot size of ~20 μm and, owing to the relative dispersions, is visually analogous to a spectroscopic isosbestic point. Also, while CE for all D_W tends to become mostly independent of spot size at values above ~90 μm, a clear bifurcation occurs between 0.9 and 1.0 mm. That is, above ~90 μm, CE is ~0.15 for $D_W \geq$ 1.0 mm but is only ~0.02 for $D_W \leq$ 0.9 mm.

The general behaviors shown in Fig. 7 again arise from the same interactions that generated the results shown in Fig. 3. Basically, a larger number of photoemission events occurring far from the x, y = 0, 0 source center point ultimately leads to a lower CE due to losses at the X-ray aperture. Further, the results suggest that, for spot sizes between roughly 20 and 100 μm, gains in CE are possible only by using a larger Wehnelt aperture, in essence by decreasing the interaction strength felt by off-axis photoelectrons. For example, in our lab, we have a 50 μm spot size on the electron source (measured externally and then extrapolated to the source),[52] we use a 1.0 mm diameter aperture, and we routinely use $h\nu$ = 4.81 eV photons for photoemission. For these conditions, the simulation results shown in Fig. 7 predict a CE of ~20% for the single-electron regime. This could be further improved to ~30% by using a 1.1 mm diameter aperture but with no further improvement for a 1.2 mm aperture. Other ways to improve CE would include using lower energy photons for photoemission, but any gains might be offset by losses arising from the reduced quantum efficiency.

CE for all three *hν*-determined E_0 distributions for select D_W

For comparison, the specific case for $h\nu$ = 4.81 eV shown in Fig. 7 was extended to the other two E_0 distributions shown in Fig. 1d. Fig. 8 displays the results for two key aperture sizes, D_W = 0.9 and 1.2 mm. We focused on these two diameters because they constitute elements of the bifurcated groupings shown in Fig. 7, and they also display significantly different dispersion behaviors with spot size for $h\nu$ = 4.81 eV. As with the highest photon energy, the two other E_0 distributions also show a general reduction in CE with increasing spot size for both apertures. The CE dispersion is again more significant for the smaller aperture, with all spot sizes above ~60 μm having the same value regardless of $h\nu$ (Fig. 8, top panel). This suggests that, for this aperture size, there is no benefit to using different incident photon energies with respect to CE for spot sizes larger than this critical value. Further, the gains below ~60 μm are less than a factor of two, suggesting reductions in beam current due to reduced quantum efficiency may outweigh any such modest gains. Compared to the 0.9 mm aperture, the dispersions for D_W = 1.2 mm are less severe, and thus the CE values with increasing spot size are more robust. Indeed, constant values for each of the E_0 distributions are seen for spot sizes up to 40 μm.

While reducing the approach into Focus Areas aids systematic study and clear reporting, practical aspects must ultimately be considered once the overall description takes shape. To a first approximation, the average UEM photoelectron beam current (I_{pe}) is given as $I_{pe} = \left[\left(\frac{E_p}{h\nu}\cdot\eta\right)\cdot \mathrm{CE}\right]\cdot e\cdot f_{rep}$, where E_p is the laser pulse energy, $h\nu$ is the photon energy, $\eta \equiv \frac{n_{pe}}{n_{h\nu}}$ is the photocathode quantum efficiency (ratio of photoelectrons emitted to photons absorbed), e is the fundamental charge, f_{rep} is the laser repetition rate, and CE is the collection efficiency defined above. Thus, one must consider multiple factors when optimizing the system for a particular application

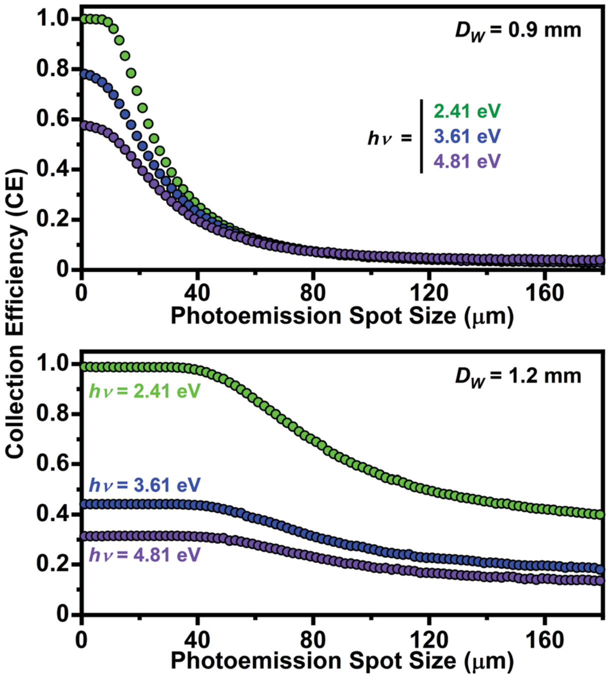

Fig. 8 Collection efficiency (CE) as a function of photoemission spot size for the E_0 distributions generated from $h\nu$ = 2.41, 3.61, and 4.81 eV for Wehnelt aperture diameters (D_W) of 0.9 mm (top panel) and 1.2 mm (bottom panel).

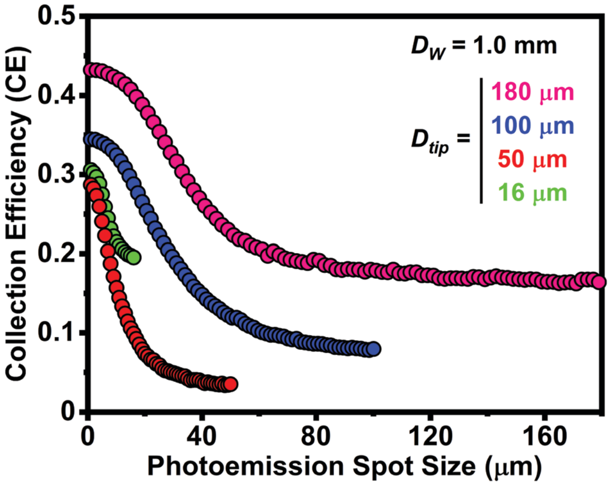

Fig. 9 Collection efficiency (CE) as a function of photoemission spot size for D_W = 1.0 mm and the $h\nu$ = 4.81 eV E_0 distribution for different D_{tip} values.

(*e.g.*, HR-UEM). For example, while values of $h\nu$ closer to Φ may give CE ∼ 1 for D_W = 1.2 mm and spot sizes below ∼40 μm (Fig. 8, bottom panel) and will also reduce the E_0 spread (Fig. 1d), the large drop in η will more than offset these gains.[62,63] Therefore, another parameter must be adjusted in order to again increase I_{pe}, likely again at the expense of another beam property. These synergistic effects illustrate the need for a detailed, methodical, and systematic approach, as taken here.

Effect of LaB$_6$ D_{tip} on CE for $h\nu$ = 4.81 eV

Finally, as seen for the temporal resolution simulations, LaB$_6$ tip diameter (D_{tip}) was also found to impact CE (Fig. 9).[12,38] This is due to variations in the pre-Wehnelt-aperture electrostatic fields along the horizontal direction at the tip surface. Four D_{tip} values were simulated for a fixed aperture size of D_W = 1.0 mm. While the qualitative behavior is approximately the same for each tip, one can see that CE at a common spot size decreases in going from D_{tip} = 180 μm to 50 μm. Interestingly, CE values are approximately the same for the two smallest tip sizes at common spot-size values, indicating the pre-aperture electrostatic fields are minimally impacted with respect to photoelectron divergence and losses at the X-ray aperture. As mentioned above, clearly a balance must be struck between factors such as beam current, temporal resolution, and coherence when considering options and weighing experimental requirements.[12] For example, while a smaller source size may provide better coherence, one may actually have a better overall beam current with a larger LaB$_6$ for a common laser spot size. In our view, insights such as these further emphasize the need to map the available parameter space and develop operational phase diagrams in order to optimize the instrument for a given set of desired conditions – the complexity hinders prediction of some of the more subtle, but nevertheless important, behaviors.

In conclusion, the systematic simulations reported here further add to the operational phase-space framework for the Tecnai Femto UEM, with the larger body of work potentially serving as a template for other 4D UEM systems. Because the focus has thus far been on easily adjustable and interchangeable laser parameters and relatively low-cost microscope elements, we anticipate being able to identify readily accessible instrument phase space for optimization of performance, depending upon the measurements of interest (*e.g.*, HR-UEM at low f_{rep} or high f_{rep} at low specimen excitation). Owing to the systematic approach and quantitative categorization of conditions and effects performed through simulations, identification and isolation of the effects of lab and instrument instabilities on the limits of resolution can be more readily determined. Future work will focus on beam coherence before building in complexity to multi-electron packets and simulations of the illumination, objective, and projection systems.

Author contributions

W. A. C. contributions were data curation, formal analysis, investigation, methodology, software, validation, visualization, writing – original draft, writing – review and editing. S. A. W. contributions were data curation, formal analysis, investigation, methodology, software, validation, visualization, writing – original draft, writing – review and editing. D. J. F. contributions were conceptualization, data curation, funding acquisition, methodology, project administration, resources, supervision, visualization, writing – original draft, writing – review and editing. See the NISO CRediT taxonomy for definitions of contributing roles (credit.niso.org).

Conflicts of interest

There are no conflicts to declare.

Acknowledgements

This material is based on work supported by the U.S. Department of Energy, Office of Science, Office of Basic Energy Sciences under Award No. DE-SC0018204. This material is based upon work supported by the National Science Foundation Graduate Research Fellowship Program under Grant No. DGE-1839286. This work was supported partially by the National Science Foundation through the University of Minnesota MRSEC under Award Number DMR-2011401. Acknowledgement is made to the Donors of the American Chemical Society Petroleum Research Fund for partial support of this research under Award No. 60584-ND10. We thank Dr Erik Kieft of Thermo Fisher Scientific for assistance with modeling the FEI Tecnai Femto architecture and for ensuring accurate electrostatic field maps were generated.

References

1 V. A. Lobastov, R. Srinivasan and A. H. Zewail, *Proc. Natl. Acad. Sci. U. S. A.*, 2005, **102**, 7069–7073.
2 H. S. Park, J. S. Baskin, O. H. Kwon and A. H. Zewail, *Nano Lett.*, 2007, **7**, 2545–2551.

3 B. Barwick, D. J. Flannigan and A. H. Zewail, *Nature*, 2009, **462**, 902–906.

4 A. H. Zewail, *Science*, 2010, **328**, 187–193.

5 D. J. Flannigan and A. H. Zewail, *Acc. Chem. Res.*, 2012, **45**, 1828–1839.

6 L. Piazza, D. J. Masiel, T. LaGrange, B. W. Reed, B. Barwick and F. Carbone, *Chem. Phys.*, 2013, **423**, 79–84.

7 L. Piazza, C. Ma, H. X. Yang, A. Mann, Y. Zhu, J. Q. Li and F. Carbone, *Struct. Dyn.*, 2014, **1**, 014501.

8 D. A. Plemmons, S. T. Park, A. H. Zewail and D. J. Flannigan, *Ultramicroscopy*, 2014, **146**, 97–102.

9 D. A. Plemmons, P. K. Suri and D. J. Flannigan, *Chem. Mater.*, 2015, **27**, 3178–3192.

10 R. M. van der Veen, T. J. Penfold and A. H. Zewail, *Struct. Dyn.*, 2015, **2**, 024302.

11 D. A. Plemmons and D. J. Flannigan, *Chem. Phys. Lett.*, 2017, **683**, 186–192.

12 K. Bikker, M. Picher, O. Cregut, T. LaGrange, B. W. Reed, S. T. Park, D. J. Masiel and F. Banhart, *Ultramicroscopy*, 2016, **171**, 8–18.

13 D. R. Cremons, D. A. Plemmons and D. J. Flannigan, *Nat. Commun.*, 2016, **7**, 11230.

14 A. Feist, N. Bach, N. Rubiano da Silva, T. Danz, M. Möller, K. E. Priebe, T. Domröse, J. G. Gatzmann, S. Rost, J. Schauss, S. Strauch, R. Bormann, M. Sivis, S. Schäfer and C. Ropers, *Ultramicroscopy*, 2017, **176**, 63–73.

15 F. Houdellier, G. M. Caruso, S. Weber, M. Kociak and A. Arbouet, *Ultramicroscopy*, 2018, **186**, 128–138.

16 L. Zhang, J. P. Hoogenboom, B. Cook and P. Kruit, *Struct. Dyn.*, 2019, **6**, 051501.

17 P. K. Olshin, M. Drabbels and U. J. Lorenz, *Struct. Dyn.*, 2020, **7**, 054304.

18 C. Zhu, D. Zheng, H. Wang, M. Zhang, Z. Li, S. Sun, P. Xu, H. Tian, Z. Li, H. Yang and J. Li, *Ultramicroscopy*, 2020, **209**, 112887.

19 D. J. Flannigan and A. H. Zewail, *Nano Lett.*, 2010, **10**, 1892–1899.

20 S. T. Park, D. J. Flannigan and A. H. Zewail, *J. Am. Chem. Soc.*, 2011, **133**, 1730–1733.

21 M. R. Armstrong, K. Boyden, N. D. Browning, G. H. Campbell, J. D. Colvin, W. J. DeHope, A. M. Frank, D. J. Gibson, F. Hartemann, J. S. Kim, W. E. King, T. B. LaGrange, B. J. Pyke, B. W. Reed, R. M. Shuttlesworth, B. C. Stuart and B. R. Torralva, *Ultramicroscopy*, 2007, **107**, 356–367.

22 A. Gahlmann, S. T. Park and A. H. Zewail, *Phys. Chem. Chem. Phys.*, 2008, **10**, 2894–2909.

23 S. T. Park, O.-H. Kwon and A. H. Zewail, *New J. Phys.*, 2012, **14**, 053046.

24 D. A. Plemmons and D. J. Flannigan, *J. Phys. Chem. A*, 2016, **120**, 3539–3546.

25 P. K. Olshin, J. M. Voss, M. Drabbels and U. J. Lorenz, *Appl. Phys. Lett.*, 2022, **120**, 104103.

26 C. Gerbig, A. Senftleben, S. Morgenstern, C. Sarpe and T. Baumert, *New J. Phys.*, 2015, **17**, 043050.

27 M. S. Grinolds, V. A. Lobastov, J. Weissenrieder and A. H. Zewail, *Proc. Natl. Acad. Sci. U. S. A.*, 2006, **103**, 18427–18431.

28 B. Barwick, H. S. Park, O.-H. Kwon, J. S. Baskin and A. H. Zewail, *Science*, 2008, **322**, 1227–1231.

29 G. S. Plows and W. C. Nixon, *J. Phys. E: Sci. Instrum.*, 1968, **1**, 595–600.

30 A. Gopinath and M. S. Hill, *IEEE Trans. Electron Devices*, 1973, **20**, 610–612.

31 T. Hosokawa, H. Fujioka and K. Ura, *Rev. Sci. Instrum.*, 1978, **49**, 1293–1299.

32 V. A. Lobastov, J. Weissenrieder, J. Tang and A. H. Zewail, *Nano Lett.*, 2007, **7**, 2552–2558.

33 W. Verhoeven, J. F.-M. van Rens, E. R. Kieft, P. H.-A. Mutsaers and O. J. Luiten, *Ultramicroscopy*, 2018, **188**, 85–89.

34 I. G.-C. Weppelman, R. J. Moerland, J. P. Hoogenboom and P. Kruit, *Ultramicroscopy*, 2018, **184**, 8–17.

35 C. Kisielowski, P. Specht, B. Freitag, E. R. Kieft, W. Verhoeven, J. F.-M. van Rens, P. Mutsaers, J. Luiten, S. Rozeveld, J. Kang, A. J. McKenna, P. Nickias and D. F. Yancey, *Adv. Funct. Mater.*, 2019, **29**, 1807818.

36 J. W. Lau, K. B. Schliep, M. B. Katz, V. J. Gokhale, J. J. Gorman, C. Jing, A. Liu, Y. Zhao, E. Montgomery, H. Choe, W. Rush, A. Kanareykin, X. Fu and Y. Zhu, *Rev. Sci. Instrum.*, 2020, **91**, 021301.

37 S. A. Reisbick, M.-G. Han, C. Liu, Y. Zhao, E. Montgomery, C. Jing, V. J. Gokhale, J. J. Gorman, J. W. Lau and Y. Zhu, *Ultramicroscopy*, 2022, **235**, 113497.

38 W. A. Curtis and D. J. Flannigan, *Phys. Chem. Chem. Phys.*, 2021, **23**, 23544–23553.

39 M. Kuwahara, S. Kusunoki, Y. Nambo, K. Saitoh, X. Jin, T. Ujihara, H. Asano, Y. Takeda and N. Tanaka, *Appl. Phys. Lett.*, 2014, **105**, 193101.

40 W. E. King, G. H. Campbell, A. Frank, B. Reed, J. F. Schmerge, B. J. Siwick, B. C. Stuart and P. M. Weber, *J. Appl. Phys.*, 2005, **97**, 111101.

41 H. Dömer and O. Bostanjoglo, *Rev. Sci. Instrum.*, 2003, **74**, 4369–4372.

42 A. V. Crewe, J. Wall and J. Langmore, *Science*, 1970, **168**, 1338–1340.

43 M. Haider, S. Uhlemann, E. Schwan, H. Rose, B. Kabius and K. Urban, *Nature*, 1998, **392**, 768–769.

44 P. E. Batson, N. Dellby and O. L. Krivanek, *Nature*, 2002, **418**, 617–620.

45 P. D. Nellist, M. F. Chisholm, N. Dellby, O. L. Krivanek, M. F. Murfitt, Z. S. Szilagyi, A. R. Lupini, A. Borisevich, W. H. Sides and S. J. Pennycook, *Science*, 2004, **305**, 1741.

46 H. Sawada, F. Hosokawa, T. Kaneyama, T. Ishizawa, M. Terao, M. Kawazoe, T. Sannomiya, T. Tomita, Y. Kondo, T. Tanaka, Y. Oshima, Y. Tanishiro, N. Yamamoto and K. Takayanagi, *Jpn. J. Appl. Phys.*, 2007, **46**, L568–L570.

47 R. Erni, M. D. Rossell, C. Kisielowski and U. Dahmen, *Phys. Rev. Lett.*, 2009, **102**, 096101.

48 E. Kieft, K. B. Schliep, P. K. Suri and D. J. Flannigan, *Struct. Dyn.*, 2015, **2**, 051101.

49 B. W. Reed, T. LaGrange, R. M. Shuttlesworth, D. J. Gibson, G. H. Campbell and N. D. Browning, *Rev. Sci. Instrum.*, 2010, **81**, 053706.
50 K. Halbach and R. F. Holsinger, *Part. Accel.*, 1976, **7**, 213–222.
51 M. J. De Loos and C. A.-J. van der Geer, *Proc. 5th Eur. Part. Acc. Conf.*, Sitges, Barcelona, Spain, 1996.
52 J. Chen and D. J. Flannigan, *Ultramicroscopy*, 2022, **234**, 113485.
53 Z. T. Pei and C. N. Berglund, *Jpn. J. Appl. Phys.*, 2002, **41**, L52–L54.
54 P. Baum, *Chem. Phys.*, 2013, **423**, 55–61.
55 M. Aidelsburger, F. O. Kirchner, F. Krausz and P. Baum, *Proc. Natl. Acad. Sci. U. S. A.*, 2010, **107**, 19714–19719.
56 C. Weninger and P. Baum, *Ultramicroscopy*, 2012, **113**, 145–151.
57 H. Ahmed and A. N. Broers, *J. Appl. Phys.*, 1972, **43**, 2185–2192.
58 S. Mogren and R. Reifenberger, *Surf. Sci.*, 1987, **186**, 232–246.
59 H. E. Gallagher, *J. Appl. Phys.*, 1969, **40**, 44–51.
60 A. A. Avdienko and M. D. Malev, *Vacuum*, 1977, **27**, 583–588.
61 E. K. Storms and B. A. Mueller, *J. Appl. Phys.*, 1979, **50**, 3691–3698.
62 K. Torgasin, K. Morita, H. Zen, K. Masuda, T. Katsurayama, T. Murata, S. Suphakul, H. Yamashita, T. Nogi, T. Kii, K. Nagasaki and H. Ohgaki, *Phys. Rev. Accel. Beams*, 2017, **20**, 073401.
63 K. Torgasin, K. Morita, H. Zen, K. Masuda, M. Bakr, K. Nagasaki, T. Kii and H. Ohgaki, *Phys. Scr.*, 2019, **94**, 075701.